International Journal of Electrical Engineering and Sustainability (IJEES)
ISSN (online): 2959-9229
https://ijees.org/index.php/ijees/index
Arab Impact Factor: 1.51 Dolj 2026 = Q1
Volume 4 | Number 2 | July-December 2026 | Pages 90-107

A Closed Form Newtonian Lubrication Model for Hydrodynamic Pressure Generation in a Combined Stepped-Tapered Wire Drawing Unit

Mohamed T. Abdlsamea[1*], Maha H. Shawish[2], Fawze A Alsaede[3]
[1]Libyan Center for Sustainable Development Research, AL-khums, Libya
[2]Libyan Center for Sustainable Development Research – Zliten Branch, Libya
[3]Libyan Center for Sustainable Development Research, AL-khums, Libya

Email:[1] moha.taher81@gmail.com, [2]mahah646@gmail.com, [3]fawzisaede@yahoo.com

Received: May 15, 2026 Accepted: July 26, 2026 Published: August 11, 2026
DOI: 10.65998/ijees.v4i2.179

Abstract: Hydrodynamic pressure generation in a combined stepped-tapered pressure unit was analysed using a deterministic closed form Newtonian lubrication model implemented in Microsoft Excel. A constant-clearance section and a linear taper were coupled through common flow and pressure continuity conditions, yielding explicit expressions for the flow rate, interface pressure, piecewise pressure field, maximum pressure, and peak location. The contribution is a compact analytical benchmark rather than a new geometry or governing theory; it separates the dimensional pressure scale μV from the geometric response governed by λ, r_1, and r_2. An independent midpoint finite-difference implementation with grid refinement produced baseline differences below 0.001%, verifying mathematical consistency but not physical validation. For the baseline geometry, P_{max} [MPa] = 1.217135S, where S = μV in Pa·m. Increasing r_2 from 10 to 18 reduced the dimensionless maximum pressure by 31.1% and shifted the peak slightly downstream. A deterministic ±5% perturbation of the outlet clearance h_3 changed P_{max} increased by 5.24% and decreased by 4.74%, respectively, while x_{max} changed by less than 0.14%. For the prescribed 2 mm solid wire, $h_1/Rw = 1.00$, $h_2/Rw = 0.50$, and $h_3/Rw = 0.05$ show that the planar approximation is not uniformly valid. The model is therefore an analytical and computational benchmark, not a geometry exact industrial design model.

Keywords: Hydrodynamic wire drawing; hydrodynamic pressure; stepped-tapered pressure unit; closed form solution; lubrication theory; finite difference verification.

1. Introduction

Wire drawing is a widely used metal forming process whose force, temperature, surface integrity, residual stress, and tool life depend on drawing speed, reduction, die geometry, friction, and material response [1-4]. Hydrodynamic lubrication reduces direct wire tool contact by entraining a viscous medium into a confined passage and generating a pressurized film. Experimental studies report improved lubricant retention, surface condition, coating preservation, and tribological performance compared with conventional arrangements [5-7].

The effectiveness of this mechanism depends on the axial pressure field, which is controlled by wire speed, viscosity, passage length, and clearance variation. Although finite-element and CFD models can represent deformation, heat transfer, and complex rheology, they require extensive data and computation. Closed form solutions remain useful for rapid sensitivity analysis and as transparent benchmarks for numerical models [8].

Earlier studies examined stepped, tapered, and combined pressure units using non-Newtonian rheology, variable viscosity, wire deformation, and experimental pressure measurement [9–12]. Recent coating flow simulations further show that shear thinning, viscoelasticity, temperature, and eccentricity can alter the response [13,14]. What remains useful is a directly evaluable, dimensionless, and reproducible constant viscosity reference for the combined geometry that isolates μV scaling, provides explicit peak relations, and states the admissible internal peak region. Such a model is a controlled benchmark rather than a complete industrial representation.

This study derives and implements in Microsoft Excel a closed form pressure solution for a constant-clearance section followed by a linear taper. The solid wire is treated as a rigid moving boundary; deformation, drawing force, thermal coupling, non-Newtonian rheology, leakage, and structural response are outside the model scope. The contribution is methodological: explicit coupled expressions, dimensionless geometric analysis, and independent finite difference verification.

The specific contributions of the study are as follows:

- A direct closed form coupling of the parallel and tapered sections through common flow and pressure-continuity conditions.
- Explicit expressions for Q, P_s, the piecewise pressure field, P_{max}, and x_{max} under constant-viscosity Newtonian assumptions.
- A dimensionless separation of the operating scale μV from the geometric effects of λ, r_1, and r_2, including the internal peak admissibility condition.
- Continuous geometric and outlet clearance tolerance sensitivity analyses, together with independent midpoint finite difference verification implemented reproducibly in Microsoft Excel.

Nomenclature

All dimensional quantities are expressed in SI units, and gauge pressure is used throughout. The symbol Q denotes volumetric flow rate per unit width under the plane flow approximation, whereas Q_a denotes a first order circumference-based estimate of annular volumetric flow rate. Dimensionless variables are defined in Section 3.9.

Table 1. Nomenclature and definitions of symbols.

Symbol	Definition	Unit
L_1	Length of the constant clearance parallel section	m
L_2	Length of the linearly tapered section	m
h_1	Constant clearance in the parallel section	m
h_2	Clearance at the inlet of the tapered section	m
h_3	Clearance at the outlet of the tapered section	m
$h(x_2)$	Local clearance within the tapered section	m
h^*	Clearance corresponding to the maximum-pressure location	m
k	Linear taper coefficient, $k = (h_2 - h_3)/L_2$	–
x	Global axial coordinate measured from the unit inlet	m
x_2	Local axial coordinate measured from the start of the tapered section	m
x_2^*	Local axial coordinate of the maximum pressure point in the tapered section	m
x_{max}	Global axial location of the maximum pressure	m
y	Coordinate across the local clearance	m
V	Wire velocity	m/s
u	Axial fluid velocity	m/s
Q	Volumetric flow rate per unit width under the plane flow approximation	m^2/s
Q_a	First order circumference based estimate of annular volumetric flow rate	m^3/s
μ	Dynamic viscosity of the pressure medium	Pa·s
ρ	Density of the pressure medium	kg/m^3
T	Operating temperature of the pressure medium	K or °C

p	Hydrodynamic gauge pressure	Pa
$p_1(x)$	Pressure distribution in the parallel section	Pa
$p_2(x_2)$	Pressure distribution in the tapered section	Pa
P_s	Interface pressure between the parallel and tapered sections	Pa
P_{max}	Maximum hydrodynamic pressure	Pa
p_{in}	Inlet gauge pressure	Pa
p_{out}	Outlet gauge pressure	Pa
dp/dx	Axial pressure gradient	Pa/m
R_w	Solid wire radius	m
D_w	Solid wire diameter, $Dw = 2Rw$	m
$R_{b,1}$	Bore radius in the parallel section	m
$R_{b,2}$	Bore radius at the tapered section inlet	m
$R_{b,3}$	Bore radius at the tapered section outlet	m
$D_{b,1}$	Bore diameter in the parallel section	m
$D_{b,2}$	Bore diameter at the tapered section inlet	m
$D_{b,3}$	Bore diameter at the tapered section outlet	m
Re_h	Film Reynolds number, $Reh = \varrho Vh/\mu$	–
ε_i	Local curvature parameter, $\varepsilon i = hi/Rw$	–
h/L	Film thickness to section length ratio used to assess the lubrication approximation	–
$\bar{x}$	Dimensionless axial position, $\bar{x} = x/(L_1 + L_2)$	–
$\bar{p}$	Dimensionless pressure, $\bar{p} = ph_3^2/(\mu VL_2)$	–
λ	Section length ratio, $\lambda = L_1/L_2$	–
r_1	Parallel-section clearance ratio, $r_1 = h_1/h_3$	–
r_2	Tapered-section inlet to outlet clearance ratio, $r_2 = h_2/h_3$	–
$\hat{q}$	Dimensionless flow parameter, $\hat{q} = 2Q/(Vh_3)$	–
η	Local dimensionless coordinate in the tapered section, $\eta = x_2/L_2$	–
H	Dimensionless local clearance, $H = h(x_2)/h_3$	–
S	Operating pressure scale parameter, $S = \mu V$	Pa·m
λ_{crit}	Critical section length ratio for an internal pressure maximum	–

2. Literature Review

2.1 Hydrodynamic Lubrication and Pressure Generation in Wire Drawing Applications

Hydrodynamic lubrication uses wire motion to entrain a viscous medium and generate a pressurized film that reduces direct contact. Experimental comparisons show lower surface roughness and residual stress, improved zinc-coating retention, and more favourable energy and tribological performance than conventional drawing [5,6,15]. Die design and lubricant selection also interact in determining drawing force and thermal stability [7].These studies establish the process benefits but provide limited explicit guidance on how wire speed, viscosity, and clearance variation determine the interface pressure, axial pressure profile, and peak location. That gap motivates a compact pressure field benchmark.

2.2 Analytical and Numerical Modelling of Stepped, Tapered, and Combined Pressure Units: Comparative Evidence and Research Gaps

Foundational work by Nwir [9], Nwir and Hashmi [12], and Akter and Hashmi [11] established tapered and combined pressure units, experimental pressure profiles, non-Newtonian rheology, variable viscosity, and wire deformation. Other analytical models focused mainly on lubricant film thickness, drawing force, or energy requirements, whereas finite element and CFD studies added thermal, deformation, viscoelastic, and three dimensional effects at greater computational cost [13-17].

2.3 Comparative Positioning and Scientific Contribution

The present study does not claim novelty in the combined geometry, Couette Poiseuille relation, or continuity conditions. Table 2 focuses on the equation level distinction: the present constant viscosity Newtonian limit provides direct expressions for the coupled flow rate, interface pressure, pressure field, and peak quantities.

Table 2. Focused equation level comparison of earlier pressure unit models and the present formulating.

Comparison criterion	Akter and Hashmi [10]	Nwir and Hashmi [12]	Akter and Hashmi [11]	Lowrie and Ngaile [16]	Present formulation
Pressure unit geometry	Two constant clearance stepped parallel sections; no tapered section.	Tapered, stepped parallel-bore, and complex/combined experimental units.	Combined parallel section followed by a linearly tapered section, with L1, L2, h1, h2, and h3.	Conical reduction die and multiple reduction die with externally supplied lubricant pressure.	Constant clearance parallel section followed by a linearly tapered section, with L1, L2, h1, h2, and h3.
Fluid rheology	Non-Newtonian Rabinowitsch model with pressure and temperature-dependent viscosity.	Viscous pressure medium used experimentally; no constitutive equation is developed in the paper.	Non-Newtonian Rabinowitsch model with variable viscosity and shear rate.	Industrial oil; lubricant properties may vary with temperature within a coupled drawing model.	Incompressible Newtonian fluid with constant dynamic viscosity.
Governing momentum relation	Pressure shear stress balance, $dp/dx = d\tau/dy$, combined with a nonlinear Rabinowitsch constitutive equation.	No governing momentum equation is derived; the study supplies experimental pressure evidence.	Pressure-shear-stress balance, $dp/dx = d\tau/dy$, combined with a nonlinear Rabinowitsch constitutive equation.	Reynolds type hydrodynamic lubrication relation coupled with deformation and thermal/material equations.	$dp/dx = \mu(\partial^2u/\partial y^2)$, with no-slip conditions at the moving wire and stationary wall.
Local velocity and flow rate relation	Nonlinear velocity and flow-rate expressions containing shear stress, pressure gradient, and variable viscosity; evaluated iteratively.	Not applicable as an experimental comparison study.	Nonlinear expressions for Q1 and Q2; continuity Q1 = Q2 is enforced through an iterative solution.	Flow and film-thickness relations are solved as part of the coupled drawing model; the primary unknown is lubricant-film thickness.	Classical Couette Poiseuille relation: $Q = Vh/2 - [h^3/(12\mu)](dp/dx)$.
Coupling between sections	Flow continuity between two stepped parallel sections; no parallel-tapered interface.	Physical behavior of different geometries is compared experimentally rather than coupled analytically.	Pressure continuity at the parallel-tapered interface and Q1 = Q2; interface quantities are obtained numerically/iteratively.	Successive reduction dies are coupled through imposed lubricant supply pressure and workpiece die conditions, not through the present stepped tapered interface.	Pressure continuity $p_1(L_1) = p_2(0) = P_s$ and common flow $Q_1 = Q_2 = Q$.
Parallel section pressure distribution	Pressure is calculated incrementally in the stepped parallel bore regions with variable viscosity.	Measured pressure profiles are reported for stepped parallel-bore and other units.	The parallel-region pressure is generated incrementally in the variable-viscosity solution.	No equivalent constant clearance upstream section matching the present geometry.	Explicit linear expression $p_1(x) = [6\mu V/h_1^2 - 12\mu Q/h_1^3]x$.

Tapered section pressure distribution	Not applicable because the model concerns a stepped parallel-bore unit.	Measured pressure distributions are reported for tapered and complex units; no closed-form equation is derived.	An analytical tapered-section relation is derived, but it contains non-Newtonian shear-stress terms and interface pressure.	Pressure/film behavior is derived for a conical reduction die.	Explicit expression $p2(x2) = (6\mu/k)\{V[1/h(x2) - 1/h3] - Q[1/h(x2)^2 - 1/h3^2]\}$.
Common flow rate solution	No explicit closed form flow rate for a combined parallel tapered unit.	Not applicable.	Q1 = Q2 is imposed, but the nonlinear shear stresses, viscosity updates, and interface pressure are solved iteratively rather than by a single geometry only closed form expression.	No counterpart to Equation (9) for the present two region geometry.	Explicit $Q = V\{(1/h2 - 1/h3) - kL1/h1^2\}/\{(1/h2^2 - 1/h3^2) - 2kL1/h1^3\}$.
Interface pressure	A step pressure exists between constant clearance regions, but it is not a parallel-tapered interface pressure.	Interface/peak pressures are measured within the tested units, not derived as a closed form coupling equation.	The parallel-tapered interface pressure is part of the coupled solution and is obtained through iterative satisfaction of Q1 = Q2.	No equivalent parallel tapered interface pressure.	Explicit $Ps = [6\mu V/h1^2 - 12\mu Q/h1^3]L1$, equivalently obtained from p2(0).
Maximum pressure condition and value	Maximum pressure is evaluated from calculated profiles; no direct closed-form peak condition was identified.	Maximum pressure is measured and compared across geometries.	Maximum pressure is obtained from theoretical/numerical pressure profiles; no explicit h* = 2Q/V expression was identified in the accessible derivation.	Film thickness and pressure behavior are solved within the drawing-die model; no equivalent explicit peak relation for this geometry.	Internal peak condition h* = 2Q/V and Pmax = p2(x2*).
Peak pressure location	Identified from computed profiles rather than a direct closed form axial location equation.	Observed from measured axial pressure profiles.	Discussed and obtained from the pressure profile; no direct explicit x* formula was identified in the accessible combined-unit derivation.	Not reported for an equivalent stepped-tapered pressure unit.	x2* = L2(h2 - h*)/(h2 - h3), with x max = L1 + x2*.
Verification or validation	Compared with earlier theoretical solutions; the article is not an independent validation of the present model.	Direct experimental pressure measurements provide an external benchmark for tapered, stepped, and complex units.	Theoretical results are compared with experiments and finite element pressure simulations.	Case-study and literature based model assessment; no direct validation of the present stepped-tapered formulation.	Independently verified using a midpoint finite difference solution with grid refinement; experimental and CFD validation have not been performed.
Equation level assessment	Different stepped geometry and a more complex non Newtonian, variable viscosity formulation.	Experimental comparator; not an analytical predecessor.	Closest predecessor; the present model is a constant-viscosity Newtonian closed-form reduction for Q, P_s, h*, P_{max}, and x_{max}.	Different geometry and coupled deformation objective.	Compact Newtonian benchmark; not the first combined geometry model or a new governing theory.

3. Model Formulation and Analytical Solution

3.1 Model Scope and Analytical Strategy

This deterministic analytical study was implemented in Microsoft Excel using prescribed inputs L_1, L_2, h_1, h_2, h_3, V, and μ. The model computes Q, P_s, p(x), P_{max}, and x_{max} for steady, laminar, incompressible, isothermal Newtonian flow. The solid wire and pressure-unit wall are treated as rigid; wire deformation, drawing force, thermal coupling, and structural response are excluded. The results are model predictions, and the planar approximation and closed-form derivation are assessed separately.

3.2 Physical Configuration

The unit comprises a constant-clearance section of length L_1 and clearance h_1 followed by a linearly converging section of length L_2, with clearance decreasing from h_2 to h_3. A solid cylindrical wire moves at constant speed V relative to the stationary wall. The global coordinate x is measured from the inlet, and x_2 from the start of the tapered section. For the present geometry, the local tapered clearance was defined as:

$$h(x_2) = h_2 - kx_2, \qquad k = (h_2 - h_3)/L_2, \qquad 0 \le x_2 \le L_2 \tag{1}$$

Equation (1) is a geometrical definition introduced for the present model. The use of parallel, tapered, and combined pressure-unit configurations is supported by earlier analytical and experimental investigations of hydrodynamic wire drawing and coating [10–12]. The inlet and outlet were assigned zero gauge pressure, $p_{in} = p_{out} = 0$, representing communication with the ambient reference pressure. This condition fixes the pressure datum and does not imply zero absolute pressure.

3.3 Modelling Assumptions

The pressure medium is assumed incompressible and Newtonian with constant viscosity. Flow is steady, laminar, isothermal, and predominantly axial; pressure is uniform across the film thickness; inertia, body forces, viscous heating, transverse velocity, and step losses are neglected. No slip conditions apply at the moving solid wire surface and stationary wall, and pressure and flow are continuous at the section interface. Under the plane flow approximation, Q denotes volumetric flow rate per unit width [16,18].

3.4 Validity of the Planar-Flow Approximation and Flow-Regime Assessment

The annular passage is approximated locally by an unwrapped planar gap. The prescribed baseline dimensions are L = 0.080 m, L_1 = 0.060 m, L_2 = 0.020 m, h_1 = 0.001 m, h_2 = 0.0005 m, h_3 = 0.00005 m, and Dw = 0.002 m, giving Rw = 0.001 m. The wire is solid; no internal diameter or wall thickness is defined. For a concentric passage, the characteristic bore radius and bore diameter at each clearance are related to the solid-wire dimensions by:

$$Rb,i = Rw + h\_i, \qquad Db,i = Dw + 2hi, \qquad i = 1, 2, 3. \tag{2}$$

The resulting baseline bore diameters are Db,1 = 0.0040 m, Db,2 = 0.0030 m, and Db,3 = 0.0021 m. The baseline ratio is $r_2 = h_2/h_3 = 10$; the parametric cases r_2 = 14 and 18 correspond to h_2 = 0.0007 and 0.0009 m, respectively. The local curvature parameter is defined as the ratio of clearance to the solid-wire radius:

$$\varepsilon i = hi/Rw = 2hi/Dw, \qquad i = 1, 2, 3. \tag{3}$$

The baseline curvature ratios are h_1/Rw = 1.00, h_2/Rw = 0.50, and h_3/Rw = 0.05; for r_2 = 14 and 18, h_2/Rw = 0.70 and 0.90. Because the upstream ratios are not much smaller than unity, the planar model is retained as a leading order benchmark rather than a geometry exact representation. Axial slenderness was assessed using h_1/L_1, h_2/L_2, and h_3/L_2 as illustrated in Table 3.

Table 3. Clearance to length ratios for the baseline geometry and parametric variants.

Location / case	Clearance	Characteristic length	Ratio	Value	Basis
Parallel section	h_1 = 0.001 m	L_1 = 0.060 m	h_1/L_1	0.0167	Baseline input
Tapered inlet: r_2 = 10	h_2 = 0.0005 m	L_2 = 0.020 m	h_2/L_2	0.0250	Baseline input
Tapered inlet: r_2 = 14	h_2 = 0.0007 m	L_2 = 0.020 m	h_2/L_2	0.0350	Parametric variant
Tapered inlet: r_2 = 18	h_2 = 0.0009 m	L_2 = 0.020 m	h_2/L_2	0.0450	Parametric variant
Tapered outlet	h_3 = 0.00005 m	L_2 = 0.020 m	h_3/L_2	0.0025	Baseline input

All clearance to length ratios are below 0.05, supporting an axial lubrication reduction; however, axial slenderness alone does not justify neglecting annular curvature. The flow regime was assessed using a film Reynolds number based on the local clearance:

$$Re\ h = \varrho Vh/\mu. \tag{4}$$

With μ ref = 100 Pa·s, V = 0.7 m/s, and h = h_1, Re hmax, ref = $7.0 \times 10^{-6}\varrho$. Across the full viscosity range, the conservative upper envelope occurs at μ = 50 Pa·s

$$Re\ h\ max = \varrho(0.7)(0.001)/50 = 1.4 \times 10^{-5}\varrho. \tag{5}$$

Because density and operating temperature are not prescribed, Equation (5) is retained as a density dependent assessment; laminar inertia free flow remains a modelling assumption rather than a material specific conclusion. Because Q in the planar formulation is a volumetric flow rate per unit width, a first-order annular estimate may be obtained by extending the planar result around the solid-wire circumference:

$$Qa \approx 2\pi RwQ = \pi DwQ. \tag{6}$$

For r_2 = 10 and V = 0.1 m/s, Q = 4.853273×10^{-6} m²/s and Qa ≈ 3.0494×10^{-8} m³/s. This first-order annular conversion is reported only as a reference because the upstream thin-annulus condition is not strongly satisfied.

Table 4. Geometric and fluid-property assessment for the prescribed computational inputs.

Quantity	Expression / basis	Prescribed or calculated value	Assessment
Total unit length, L	$L_1 + L_2$	0.080 m	Prescribed
Solid-wire diameter, Dw	Prescribed diameter	0.002 m	Used in hydraulic curvature assessment
Solid wire radius, Rw	Dw/2	0.001 m	Calculated
Parallel section bore diameter, Db,1	Dw + $2h_1$	0.0040 m	Calculated
Tapered inlet bore diameter, Db,2	Dw + $2h_2$	0.0030 m	Baseline r_2 = 10
Tapered outlet bore diameter, Db,3	Dw + $2h_3$	0.0021 m	Calculated
Baseline curvature ratios	h_1/Rw; h_2/Rw; h_3/Rw	1.00; 0.50; 0.05	Calculated; planar approximation not uniformly valid
Reference viscosity, μ ref	Supplied value	100 Pa·s	Prescribed baseline value
Pressure medium density, ϱ	Required for Re h	Not specified	Material specific assessment incomplete
Operating temperature, T	Associated with μ and ϱ	Not supplied	Material-specific assessment incomplete
Maximum Reynolds number	$1.4 \times 10^{-5}\varrho$	Density dependent	Cannot be finalized without ϱ
First order annular flow estimate, Q_a	πDwQ at V = 0.1 m/s	3.0494×10^{-8} m³/s	Circumference based estimate; curvature limitation applies

3.5 Pressure-Medium Properties and Validity of the Newtonian Assumption

The pressure medium is modelled as an incompressible Newtonian fluid. The reference value μ ref = 100 Pa·s and the parametric values 50 and 150 Pa·s are prescribed computational inputs, not measured properties of a specified commercial medium. Accordingly, the results represent constant-viscosity model responses rather than material specific industrial predictions. The applicability of the constant viscosity assumption depends on pressure, temperature, and characteristic shear rate. A first order shear rate scale is

$$\dot{\gamma}c \approx V/h$$

Using the smallest clearance $h_3 = 5.0 \times 10^{-5}$ m and wire speeds of 0.1–0.7 m/s gives $2.0 \times 10^3 \leq \dot{\gamma}\_c \leq 1.4 \times 10^4\ s^{-1}$.

The estimated shear rate range is 2.0×10^3–1.4×10^4 s^{-1}. Real polymeric media may therefore exhibit shear thinning, pressure dependent viscosity, or viscous heating; the exact μV scaling applies only to the Newtonian, isothermal benchmark.

3.6 Governing Fluid-Flow Equations

Under the stated assumptions, the axial Navier Stokes equation reduces to the one-dimensional lubrication relation in Equation (7) [16,18].

$$dp/dx = \mu(\partial^2 u/\partial y^2) \quad (7)$$

Here, p is hydrodynamic pressure, u is axial fluid velocity, x is the axial coordinate, y is the coordinate across the local clearance h, and μ is the dynamic viscosity. The no-slip boundary conditions are:

$$u(x,0) = V,\ u(x,h) = 0 \quad (8)$$

Integrating Equation (7) twice with respect to y and applying Equation (8) gives the combined Couette Poiseuille velocity profile:

$$u(y) = V(1 - y/h) + [1/(2\mu)](dp/dx)(y^2 - hy) \quad (9)$$

Equation (9) is derived in the present study from the cited lubrication equation and boundary conditions. Integrating the velocity across the clearance gives the flow rate per unit width:

$$Q = \int_0^h u(y)dy = Vh/2 - [h^3/(12\mu)](dp/dx) \quad (10)$$

Rearrangement of Equation (10) yields the pressure-gradient relation used throughout the model:

$$dp/dx = 6\mu V/h^2 - 12\mu Q/h^3 \quad (11)$$

Equations (9),(11) are the standard plane Couette Poiseuille relations applied here to the stepped-tapered geometry.

3.7 Closed Form Pressure Solution

3.7.1 Parallel Section

In the parallel section, $h = h_1$ is constant. Applying $p_1(0) = 0$ and integrating Equation (11) gives:

$$p_1(x) = [6\mu V/h_1^2 - 12\mu Q/h_1^3]x,\ 0 \le x \le L_1 \quad (12)$$

The interface pressure is $P_s = p_1(L_1)$.

3.7.2 Tapered Section

In the tapered section, h varies according to Equation (1). Substituting $h(x_2)$ into Equation (11), integrating, and applying $p_2(L_2) = 0$ gives:

$$p_2(x_2) = (6\mu/k)\{V[1/h(x_2) - 1/h_3] - Q[1/h(x_2)^2 - 1/h_3^2]\} \quad (13)$$

Equation (13) is the closed form tapered section solution obtained from Equation (11) and the linear clearance profile.

3.7.3 Flow Continuity and Interface Pressure

The same flow rate Q was imposed in both sections, and pressure continuity was required at the interface: $Q_1 = Q_2 = Q$ and $p_1(L_1) = p_2(0) = P_s$. Solving these two conditions gives the closed form flow rate:

$$Q = V\{(1/h_2 - 1/h_3) - kL_1/h_1^2\}/\{(1/h_2^2 - 1/h_3^2) - 2kL_1/h_1^3\} \quad (14)$$

The interface pressure can then be evaluated from either section:

$$P_s = [6\mu V/h_1^2 - 12\mu Q/h_1^3]L_1 \quad (15)$$

or equivalently from Equation (13) at $x_2 = 0$. The complete axial pressure field is therefore:

$$p(x) = p_1(x),\ 0 \le x \le L_1;\ p(x) = p_2(x - L_1),\ L_1 < x \le L_1 + L_2 \quad (16)$$

Equations (14) ,(16) follow directly from common flow and pressure-continuity conditions at the interface.

3.8 Determination of Maximum Pressure

The local maximum is obtained by setting the pressure gradient in Equation (11) to zero, giving the clearance at the pressure peak:

$$h^* = 2Q/V \tag{17}$$

When $h_3 < h^* < h_2$, the peak lies inside the tapered section. Its local and global axial positions are:

$$x_2^* = L_2(h_2 - h^*)/(h_2 - h_3) \tag{18}$$

$$x_{max} = L_1 + x_2^* \tag{19}$$

The corresponding maximum pressure is:

$$P_{max} = p_2(x_2^*) \tag{20}$$

Equations (17),(20) follow from $dp/dx = 0$ and the linear clearance profile; otherwise the maximum is determined from the boundary values.

3.9 Dimensionless Formulation and Geometric Admissibility

For fixed geometry, Q is proportional to V and pressure is proportional to μV. The following dimensionless form separates this operating scale from the geometric response.

3.9.1 Dimensionless Variables

The dimensionless axial coordinate, pressure, section-length ratio, and clearance ratios are defined as:

$$\bar{x} = x/(L_1 + L_2), \quad \bar{p} = ph_3^2/(\mu V L_2), \quad \lambda = L_1/L_2, \quad r_1 = h_1/h_3, \quad r_2 = h_2/h_3. \tag{21}$$

A dimensionless flow parameter is also introduced as

$$\hat{q} = 2Q/(Vh_3). \tag{22}$$

Substitution of the dimensional closed-form flow-rate relation gives

$$\hat{q} = 2[(1 - 1/r_2) + (r_2 - 1)\lambda/r_1^2] \,/\, [(1 - 1/r_2^2) + 2(r_2 - 1)\lambda/r_1^3]. \tag{23}$$

Equation (23) depends only on λ, r_1, and r_2; μV sets the dimensional pressure scale.

3.9.2 Dimensionless Pressure Distribution

For the tapered section, define the local coordinate and dimensionless clearance as

$$\eta = x_2/L_2, \quad H(\eta) = h(x_2)/h_3 = r_2 - (r_2 - 1)\eta. \tag{24}$$

The dimensionless pressure in the parallel section is

$$\bar{p}_1(\bar{x}) = 6(\lambda + 1)\bar{x}(1/r_1^2 - \hat{q}/r_1^3). \tag{25}$$

The dimensionless pressure in the tapered section is

$$\bar{p}_2(\eta) = 6/(r_2 - 1)[(1/H - 1) - (\hat{q}/2)(1/H^2 - 1)]. \tag{26}$$

The corresponding dimensionless interface pressure is

$$\bar{P}_s = 6\lambda(1/r_1^2 - \hat{q}/r_1^3). \tag{27}$$

Cases with the same λ, r_1, and r_2 therefore have the same normalized pressure distribution.

3.9.3 Geometric Admissibility of an Internal Pressure Maximum

The dimensional condition $h^* = 2Q/V$ becomes

$$h^*/h_3 = \hat{q}. \tag{28}$$

An internal maximum lies within the tapered section only when

$$1 < \hat{q} < r_2. \tag{29}$$

For $r_1 \le r_2$, the upper inequality is automatically satisfied. For $r_1 > r_2$, it gives Equation (30).

$$\lambda < \lambda crit = r_1^3(r_2 - 1)/[2r_2(r_1 - r_2)], \quad \text{for } r_1 > r_2. \tag{30}$$

Cases with $\lambda \ge \lambda crit$ do not have an internal tapered-section peak; the maximum must then be taken from the boundaries.

3.9.4 Dimensionless Peak Location and Maximum Pressure

When the admissibility condition is satisfied, the local peak position in the tapered section is

$$\eta^* = (r_2 - \hat{q})/(r_2 - 1). \tag{31}$$

The corresponding normalized global axial location is

$$\bar{x}_{max} = [\lambda + (r_2 - \hat{q})/(r_2 - 1)]/(\lambda + 1). \tag{32}$$

Substitution of $H = \hat{q}$ into the tapered-section pressure expression gives the dimensionless maximum pressure

$$\bar{p}_{max} = 3(\hat{q} + 1/\hat{q} - 2)/(r_2 - 1). \tag{33}$$

The dimensional maximum pressure is recovered from

$$P_{max} = (\mu V L_2/h_3^2)\bar{p}_{max}. \tag{34}$$

Equation (34) separates the operating scale μV from the geometric maximum $\bar{p}_{max}$.

3.9.5 Baseline Dimensionless Evaluation and Revised Analysis Strategy

For the baseline inputs,

$$\lambda = 3, \quad r_1 = 20, \quad r_2 \in \{10, 14, 18\}. \tag{35}$$

The dimensionless results for the three reported tapered-section ratios are summarized in Table 5.

Table 5. Dimensionless baseline results for the investigated tapered-section clearance ratios.

r_2	$\hat{q}$	$\bar{p}_s$	$\bar{p}_{max}$	$\bar{x}_{max}$	Internal-peak condition
10	1.94131	0.04063	0.15214	0.97385	Satisfied
14	2.04265	0.04040	0.12282	0.97995	Satisfied
18	2.12337	0.04022	0.10488	0.98348	Satisfied

Over the investigated interval, increasing r_2 reduces the dimensionless maximum pressure and moves the peak downstream, whereas the dimensionless interface pressure changes only slightly because the upstream geometry remains fixed. Accordingly, the numerical evaluation was reorganized into one exact operating scale analysis based on $S = \mu V$, continuous geometric sweeps of r_2, λ, and r_1, and an admissibility map for the internal pressure maximum. The wider λ and r_1 intervals used in the sensitivity study are analytical design ranges introduced to examine model behavior; they are not measured industrial operating limits.

3.10 Parametric Analysis

The evaluation used three complementary components. First, speed and viscosity were represented by the exact operating scale $S = \mu V = 5–105$ Pa·m. Second, continuous sweeps examined $10 \le r_2 \le 18$ at $\lambda = 3$ and $r_1 = 20$, $0.5 \le \lambda \le 10$ at $r_1 = 20$ and $r_2 = 10$, and $10 \le r_1 \le 30$ at $\lambda = 3$ and $r_2 = 10$. An admissibility map used $2 \le r_2 \le 18$ and $0 \le \lambda \le 400$ at $r_1 = 20$. Third, a deterministic tolerance analysis perturbed h_3 by ±1% and ±5% about its 50 μm baseline while holding L_1, L_2, h_1, h_2, V, and μ fixed. These are analytical evaluations, not measured industrial limits or a probabilistic uncertainty model.

Table 6. Continuous evaluation plan for operating-scale and geometric analyses.

Analysis	Fixed quantities	Varied quantity / range	Primary outputs
Operating scale	$\lambda = 3$, $r_1 = 20$, $r_2 = 10$	$S = \mu V = 5–105$ Pa·m	P_s, P_{max}, x_{max}
Tapered clearance	$\lambda = 3$, $r_1 = 20$	$10 \le r_2 \le 18$	$\hat{q}$, $\bar{p}_s$, $\bar{p}_{max}$, $\bar{x}_{max}$
Section lengths	$r_1 = 20$, $r_2 = 10$	$0.5 \le \lambda \le 10$	$\bar{p}_{max}$, $\bar{x}_{max}$
Parallel clearance	$\lambda = 3$, $r_2 = 10$	$10 \le r_1 \le 30$	$\bar{p}_{max}$, $\bar{x}_{max}$
Admissibility map	$r_1 = 20$	$2 \le r_2 \le 18$; $0 \le \lambda \le 400$	Internal-peak region and λcrit
Outlet-clearance tolerance	L_1, L_2, h_1, h_2, $V = 0.1$ m/s, $\mu = 100$ Pa·s	h_3: −5%, −1%, baseline, +1%, +5%	P_{max}, ΔP_{max}, x_{max}

The dimensional outputs were P_s, P_{max}, and x_{max}; the dimensionless outputs were $\hat{q}$, $\bar{P}_s$, $\bar{p}_{max}$, and $\bar{x}_{max}$. The tolerance analysis additionally reported the percentage change in P_{max} relative to the baseline. All calculations used double precision, with dimensional pressure recovered from $P = (\mu V L_2/h_3^2)\bar{p}$.

3.11 Computational Implementation and Reproducibility

The Microsoft Excel workbook contains separate blocks for prescribed inputs, closed-form calculations, dimensionless analysis, finite difference verification, and figure data. It checks inlet and outlet pressure, interface pressure continuity, common flow continuity, peak admissibility, and analytical numerical differences.

3.12 Equation Provenance and Analytical Traceability

To make the origin of the equations transparent to reviewers, Table 7 distinguishes established governing theory from equations derived specifically for this study.

Table 7. Equation provenance and analytical traceability.

Equation(s)	Provenance	Supporting source or derivation
(1)	Present-study definition	Linear clearance profile for the selected stepped-tapered geometry; geometry precedent: Akter and Hashmi [11].
(2)–(6)	Geometric definitions and assessment	Bore geometry, curvature ratio, film Reynolds number, and first-order annular-flow conversion based on the supplied dimensions.
(7)–(8)	Established theory	Thin film reduction of Navier Stokes and no-slip boundary conditions; Lowrie and Ngaile [16]; Pusterhofer et al. [18].
(9)–(11)	Derived from established theory	Couette–Poiseuille velocity, flow-rate, and pressure-gradient relations obtained from Equations (7)–(8).
(12)–(13)	Present-study derivation	Closed-form pressure solutions for the constant and linearly varying clearances.
(14)–(16)	Present-study derivation	Coupled flow rate, interface pressure, and piecewise pressure field obtained from flow and pressure continuity; combined unit precedent: Akter and Hashmi [11].
(17)–(20)	Present-study derivation	Maximum-pressure condition, location, and value obtained from dp/dx = 0 and the linear clearance function.
(21)–(35)	Present-study reformulation	Dimensionless variables, pressure field, admissibility condition, and peak relations derived from the dimensional closed-form model.
(36)	Independent numerical discretization	Midpoint finite-difference approximation of the governing pressure-gradient equation used for verification.

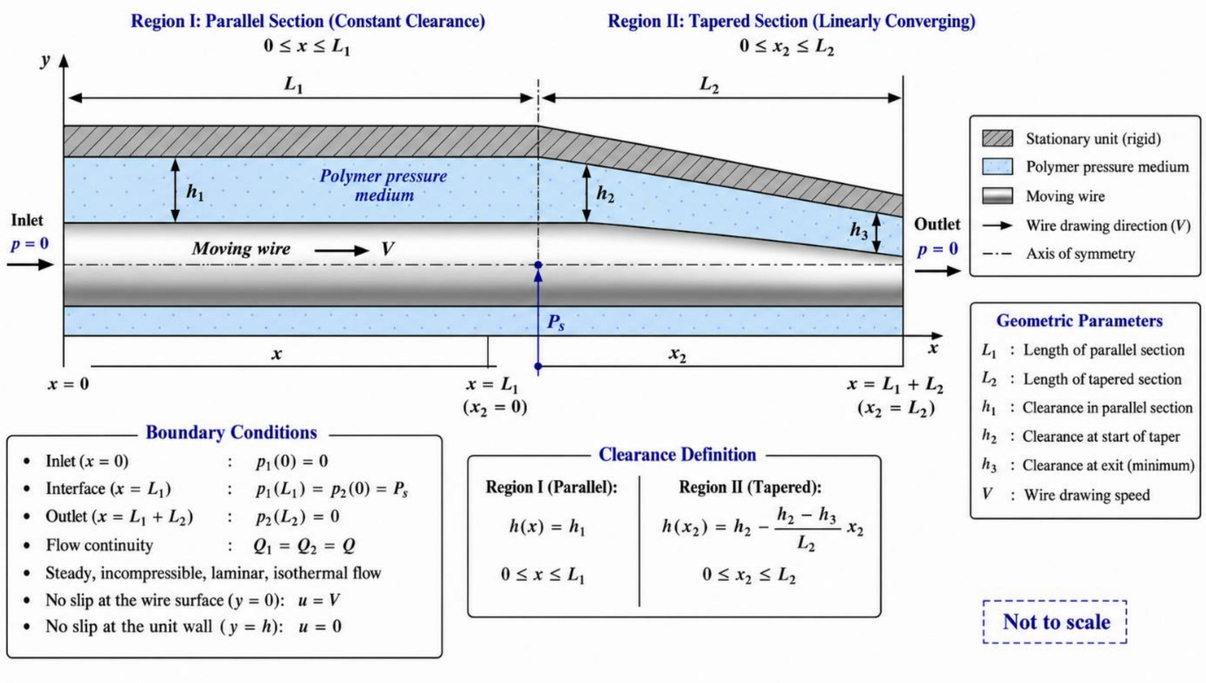

Figure 1. Schematic axial section of the combined stepped-tapered hydrodynamic pressure unit.

Region I represents the constant clearance parallel section, whereas Region II represents the linearly converging section. The pressure solutions are coupled through pressure and flow continuity at the interface.

4. Independent Finite Difference Verification

4.1 Numerical Procedure

The governing pressure-gradient equation was independently discretized by a midpoint finite-difference scheme in Microsoft Excel. The calculation used only the prescribed geometry, boundary conditions, and discretized governing equation; it did not call the closed form pressure or peak expressions. The domain $L = L_1 + L_2$ was divided into N uniform intervals of size Δx, with clearance evaluated at each midpoint.

For each interval i, the governing equation was discretized as

$$(p_{i+1} - p_i)/\Delta x = 6\mu V/h_{i+1/2}^2 - 12\mu Q/h_{i+1/2}^3. \tag{36}$$

The unknown common flow rate was determined from $p_0 = p_N = 0$. P_s was extracted at $x = L_1$, and P_{max} and x_{max} were obtained from the numerical pressure field using local quadratic interpolation.

Algorithm 1. Independent finite-difference implementation

Figure 1. Define L_1, L_2, h_1, h_2, h_3, V, μ, and N.

Figure 2. Generate the uniform grid and evaluate the midpoint clearance in each interval.

Figure 3. Determine Q from the discrete inlet-to-outlet pressure-closure condition.

Figure 4. Integrate the discrete pressure gradient from $p_0 = 0$ to obtain the nodal pressures.

Figure 5. Extract P_s at $x = L_1$ and determine P_{max} and x_{max} from the numerical field.

Figure 6. Repeat on refined grids and calculate the relative differences from the closed form solution.

4.2 Baseline Case and Grid Refinement Assessment

The baseline case used $L_1 = 0.06$ m, $L_2 = 0.02$ m, $h_1 = 0.001$ m, $h_2 = 0.0005$ m, $h_3 = 0.00005$ m, $V = 0.1$ m/s, and $\mu = 100$ Pa·s. Grids of N = 800, 1600, 3200, 8000, and 16000 were tested. At N = 8000 ($\Delta x = 1.0 \times 10^{-5}$ m), all reported differences were below 0.001%.

Table 8. Independent finite-difference verification of the closed-form solution for the baseline case

Quantity	Closed-form solution	Finite-difference solution (N = 8000)	Relative difference (%)
Flow rate per unit width, Q (m²/s)	4.853273×10^{-6}	4.853289×10^{-6}	0.000334
Interface pressure, P_s (MPa)	3.250564	3.250563	0.000036
Maximum pressure, P_{max} (MPa)	12.171348	12.171309	0.000320
Peak location, x_{max} (m)	0.07790820	0.07790817	0.000038

Table 9. Grid refinement assessment for the independent finite difference solution

Number of intervals, N	Δx (m)	P_{max} (MPa)	Relative difference in P_{max} (%)	x_{max} (m)
800	1.00×10^{-4}	12.167427	0.032215	0.07790505
1600	5.00×10^{-5}	12.170365	0.008071	0.07790745
3200	2.50×10^{-5}	12.171102	0.002018	0.07790805
8000	1.00×10^{-5}	12.171309	0.000320	0.07790817
16000	5.00×10^{-6}	12.171338	0.000080	0.07790820

Refinement from N = 800 to 16000 reduced the maximum pressure difference from 0.032215% to 0.000080%, demonstrating systematic convergence to the closed form solution.

4.3 Verification and Validation Status

The finite-difference results verify the derivation and implementation under the same Newtonian, isothermal, plane flow assumptions. They do not constitute experimental or CFD validation.

5. Results

Results are organized by the exact operating scale μV, followed by continuous geometric sensitivity and peak admissibility.

5.1 Exact Operating Parameter Scaling Through μV

For the baseline geometry $\lambda = 3$, $r_1 = 20$, and $r_2 = 10$, the dimensionless quantities are $\hat{q} = 1.94131$, $\bar{p}_s = 0.040632$, $\bar{p}_{max} = 0.152142$, and $\bar{x}_{max} = 0.973853$. Consequently, the dimensional interface and maximum pressures are determined exactly by the single operating scale parameter $S = \mu V$:

$$P_s = 0.325056\, S \ \text{(MPa)}, \quad P_{max} = 1.217135\, S \ \text{(MPa)},$$

when S is expressed in Pa·m. The peak location remains x_{max} = 0.077908 m for every μ–V combination having this geometry. Thus, speed and constant viscosity do not constitute independent geometric sensitivities in the present Newtonian model; combinations with the same μV generate the same pressure field.

Table 10. Representative dimensional pressures for selected values of μV.

μV (Pa·m)	P_s (MPa)	P_{max} (MPa)	x_{max} (m)
5	1.625	6.086	0.077908
10	3.251	12.171	0.077908
40	13.002	48.685	0.077908
70	22.754	85.199	0.077908
105	34.131	127.799	0.077908

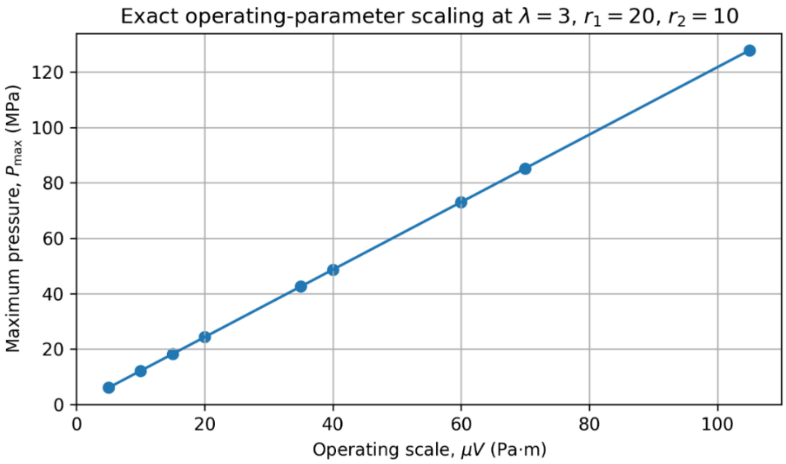

Figure 2. Exact linear scaling of the maximum pressure with μV for the baseline geometry. The plotted points correspond to representative combinations from the original speed viscosity parameter set.

5.2 Continuous Influence of the Tapered-Section Clearance Ratio

At λ = 3 and r_1 = 20, increasing r_2 from 10 to 18 reduced $\tilde{p}_{max}$ from 0.152142 to 0.104880 (31.1%) and shifted $\tilde{x}_{max}$ from 0.973853 to 0.983480. $\tilde{P}_s$ changed only slightly because the upstream geometry was fixed. The response is monotonic; no optimum is claimed without additional constraints.

Table 11. Dimensionless benchmark values within the continuous r_2 sweep.

r_2	$\tilde{q}$	$\tilde{p}_s$	$\tilde{p}_{max}$	$\tilde{x}_{max}$
10	1.94131	0.040632	0.152142	0.973853
14	2.04265	0.040404	0.122817	0.979949
18	2.12337	0.040222	0.104880	0.983480

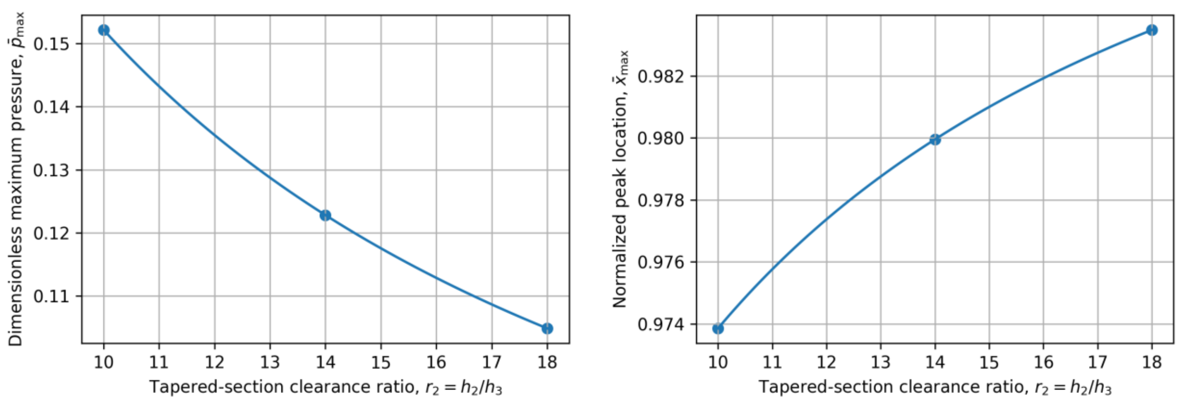

(a) Dimensionless maximum pressure. **(b)** Normalized peak location.

Figure 3. Continuous effect of r_2 over the investigated interval at $\lambda = 3$ and $r_1 = 20$. The markers identify the originally reported values $r_2 = 10$, 14, and 18.

5.3 Continuous Sensitivity to λ and r₁

At $r_1 = 20$ and $r_2 = 10$, increasing λ from 0.5 to 10 raised p^{*}_{max} from 0.127549 to 0.224074 (75.7%) and moved x^{*}_{max} from 0.937865 to 0.987654. At $\lambda = 3$ and $r_2 = 10$, increasing r_1 from 10 to 30 reduced p^{*}_{max} from 0.229178 to 0.136111 (40.6%) and moved x^{*}_{max} from 0.965517 to 0.975694.

Table 12. Endpoint sensitivity over the analytical λ and r_1 ranges

Sweep	Lower endpoint	Upper endpoint	p^{*}_{max} change	x^{*}_{max} change
λ	0.5: 0.127549	10: 0.224074	+75.7%	0.937865 → 0.987654
r_1	10: 0.229178	30: 0.136111	−40.6%	0.965517 → 0.975694

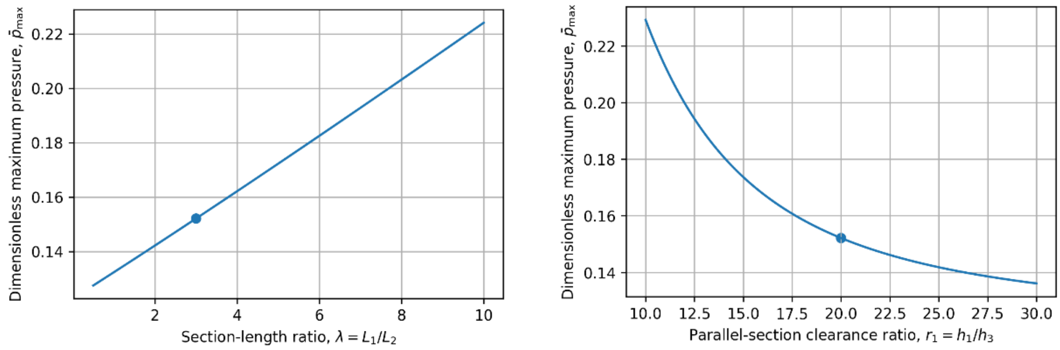

(a) Sensitivity to λ at $r_1 = 20$ and $r_2 = 10$. **(b)** Sensitivity to r_1 at $\lambda = 3$ and $r_2 = 10$.

Figure 4. Continuous geometric sensitivity of the dimensionless maximum pressure. The markers denote the baseline values $\lambda = 3$ and $r_1 = 20$.

5.4 Geometric Admissibility of the Internal Pressure Maximum

An internal maximum in the tapered section requires $1 < q^{*} < r_2$. For $r_1 = 20$ and $r_2 < 20$, this condition is equivalent to $\lambda < \lambda crit$. The critical values are 360.0, 619.05, and 1888.89 for $r_2 = 10$, 14, and 18, respectively; therefore, the baseline $\lambda = 3$ lies well inside the internal peak region for all investigated cases.

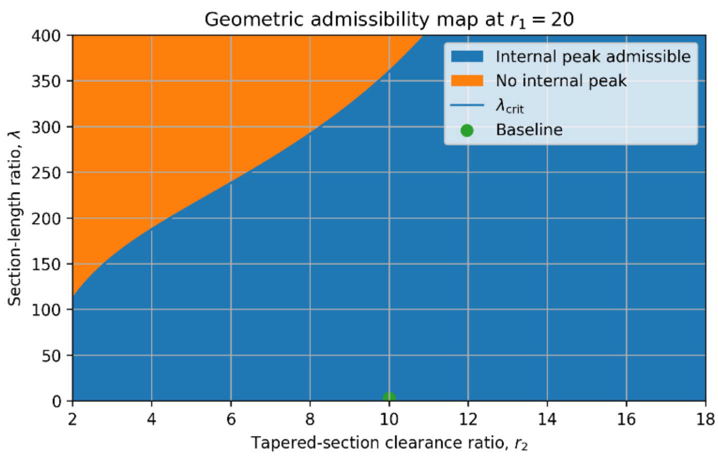

Figure 5. Geometric admissibility map for an internal pressure maximum at $r_1 = 20$. The shaded region below $\lambda crit$ satisfies $1 < q^{*} < r_2$; the marker shows the baseline geometry.

5.5 Outlet Clearance Tolerance Sensitivity

Because h_3 enters both the dimensional pressure scale and the geometric ratios, small outlet-clearance changes materially affect the predicted peak pressure. Reducing h_3 by 5% increased P_{max} from 12.171 to 12.809 MPa (+5.24%), whereas increasing h_3 by 5% reduced it to 11.594 MPa (−4.74%). A ±1%

perturbation changed P_{max} by approximately 1% in the opposite direction, while x_{max} changed by less than 0.14% even at ±5%. The peak magnitude is therefore approximately first order sensitive to outlet clearance, whereas the peak location is comparatively robust. This is a deterministic sensitivity test and does not replace a measured tolerance distribution.

Table 13. Deterministic sensitivity of the baseline solution to outlet-clearance variation

h_3 variation	h_3 (μm)	P_{max} (MPa)	ΔP_{max} (%)	x_{max} (mm)
−5%	47.5	12.809	+5.24	78.017
−1%	49.5	12.294	+1.01	77.930
Baseline	50.0	12.171	0.00	77.908
+1%	50.5	12.051	−0.99	77.886
+5%	52.5	11.594	−4.74	77.799

6. Discussion

The principal analytical result is the exact separation of the operating scale from the geometric response. For fixed λ, r_1, and r_2, the model gives $P \propto \mu V$, while the normalized pressure profile and peak location are independent of the individual values of μ and V. This proportionality should be interpreted as a mathematical consequence of the constant viscosity Newtonian formulation, not as a newly discovered material law. Earlier experimental and non Newtonian studies similarly identified wire speed, viscosity, and pressure-unit geometry as primary controls on pressure generation [11,12], but their variable viscosity, shear-rate dependence, and wire deformation permit nonlinear departures from the present scaling. The value of the current result is therefore that it provides a transparent reference against which those departures can be quantified.

The reduction in dimensionless maximum pressure as r_2 increased from 10 to 18 can be explained directly from the coupled geometry. The dimensionless flow parameter increased only modestly, from 1.94131 to 2.12337, whereas the tapered clearance range r_2-1 increased substantially; consequently, the geometric pressure amplification term decreased and $p_{\circledcirc max}$ fell by 31.1%. The near outlet peak is also a consequence of the pressure-gradient condition. In the tapered section, dp/dx changes sign when $h = h^* = 2Q/V$. For the investigated cases, $h^*/h_3 = q_{\circledcirc} \approx 1.94–2.12$, which places h^* much closer to h_3 than to h_2. Pressure therefore rises through most of the taper and falls only over the short downstream interval after h reaches h^*. Increasing r_2 moves the normalized peak slightly farther downstream because the inlet clearance increases more rapidly than h^*. This behavior is qualitatively consistent with earlier experimental profiles in which the maximum occurred in the downstream part of the pressure unit [9,12].

The λ and r_1 sensitivities have distinct physical interpretations. Increasing λ from 0.5 to 10 raised $p_{\circledcirc max}$ by 75.7% because a longer constant clearance section accumulates a larger interface pressure before the flow enters the taper. In contrast, increasing r_1 from 10 to 30 reduced $p_{\circledcirc max}$ by 40.6%; a larger upstream clearance lowers viscous resistance and weakens pressure buildup. The h_3 tolerance analysis reinforces the importance of clearance control: a ±5% perturbation changed P_{max} by approximately +5.24%, −4.74%, but changed x_{max} by less than 0.14%. These trends agree qualitatively with earlier combined-unit studies showing that relative passage dimensions govern pressure magnitude and distribution [11,12]. The present contribution is their explicit dimensionless and tolerance based quantification. Because the responses are monotonic and no structural, thermal, leakage, or process performance constraint is imposed, the analysis identifies sensitivity rather than an optimum design.

The predicted pressure magnitudes require cautious comparison with the experimental literature. The present baseline gives P_{max} = 12.17 MPa at V = 0.1 m/s and μ = 100 Pa·s, whereas the highest investigated operating scale gives 127.80 MPa. The doctoral experimental record underpinning the later journal work reported a peak of almost 1500 bar (approximately 150 MPa) at 0.13 m/s in a tapered unit for a particular gap ratio and non-Newtonian pressure medium [9], while Nwir and Hashmi [12] compared tapered, stepped, and complex units experimentally. Thus, the upper prediction is of the same order as earlier plasto hydrodynamic pressures, whereas the baseline value is substantially lower.

The current pressure-only model should also be distinguished from studies reporting process-level benefits. Hydrodynamic dies have been associated experimentally with improved lubricant retention, surface condition, coating preservation, reduced residual stress, and favourable energy or tribological performance [5–7,15]. Those outcomes depend on coupled pressure, friction, temperature, material deformation, and lubricant behaviour. The present formulation isolates only the pressure generation mechanism; it cannot establish that a higher pressure necessarily reduces drawing force, improves coating quality, or produces wire reduction. This distinction is important because the 127.80 MPa result is a hydraulic prediction under prescribed assumptions, not evidence of an acceptable or superior operating condition.

The supplied solid wire dimensions expose the principal geometric limitation of the formulation. Although the clearance to length ratios are below 0.05, the upstream curvature ratios $h_1/Rw = 1.00$ and $h_2/Rw = 0.50$ are not asymptotically small. The closed form plane flow solution may therefore differ materially from an exact annular solution in both flow rate and pressure. More detailed studies have incorporated axisymmetric or conical geometry, variable viscosity, deformation, heat transfer, viscoelasticity, and eccentricity [11,13,14,16]. Their greater physical realism explains why the present solution should be used as a leading-order benchmark. Similarly, the estimated shear-rate range indicates that the prescribed constant viscosities may not represent real polymer melts, so the exact μV scaling should not be extrapolated to non-Newtonian or thermally coupled operation.

Finally, the midpoint finite-difference solution provides strong evidence of mathematical and computational consistency: grid refinement reduced the maximum-pressure difference to 0.000080%, and all baseline quantities agreed within 0.001%. Because the numerical route used the same governing assumptions, this agreement verifies the derivation but does not establish physical validity. A point by point quantitative comparison with published measurements is not claimed because the available experimental cases use different geometries, fluids, temperatures, and deformable wires. Accordingly, the defensible contribution is a concise, reproducible Newtonian reference solution that exposes operating and geometric scaling and can support future comparison with axisymmetric, non-Newtonian, CFD, structural, and experimental models.

7. Limitations and Future Work

The model assumes steady, incompressible, isothermal Newtonian flow with constant viscosity and neglects annular curvature in the governing equations, entrance and exit effects, step losses, leakage, roughness, eccentricity, wall slip, compressibility, cavitation, viscoelasticity, pressure-dependent viscosity, and viscous heating. The prescribed geometry shows that the planar approximation is not uniformly valid.

The solid wire and pressure-unit wall are rigid, and structural response is outside the model. Finite-difference agreement verifies only the mathematics under the same assumptions. The parameter ranges are analytical rather than validated industrial limits, and the tolerance study is deterministic, limited to h_3, and unsupported by measured manufacturing distributions or covariance among dimensions.

Future work should compare the benchmark with an axisymmetric annular model or validated CFD, characterize a specific pressure medium, obtain pressure measurements, and perform structural assessment before constrained design optimization.

8. Conclusion

A closed-form Newtonian lubrication benchmark was developed for a constant-clearance section followed by a linear taper and implemented reproducibly in Microsoft Excel. The model provides explicit Q, P_s, p(x), P_{max}, and x_{max} relations, separates the pressure scale μV from the geometric response, and was independently verified by a convergent midpoint finite-difference calculation with baseline differences below 0.001%.

For the baseline geometry, P_{max} [MPa] = 1.217135S, where S = μV in Pa·m. Increasing r_2 from 10 to 18 reduced p_{max} by 31.1%, and a ±5% change in h_3 changed P_{max} by approximately +5.24%, −4.74% while altering x_{max} by less than 0.14%. Because the prescribed solid-wire geometry does not satisfy the planar curvature criterion uniformly, the solution is suitable for analytical screening and numerical benchmarking, not direct industrial design.

Author Contributions: Authors have contributed significantly to the development and completion of this article.
Funding: This article received no external funding.
Data Availability Statement: Not applicable.

Data and Code Availability: All analytical, dimensionless, finite difference, tolerance sensitivity, table, and figure calculations were implemented in Microsoft Excel.

Acknowledgments: The author would like to express their sincere gratitude to Libyan Center for Sustainable Development Research, AL-khums, Libya for their invaluable support and resources throughout the course of this research.
Conflicts of Interest: The author(s) declare no conflict of interest.

References

[1] G. A. Santana Martinez, W.-L. Qian, L. K. Kabayama, and U. Prisco, "Effect of process parameters in copper-wire drawing," Metals, vol. 10, no. 1, Art. no. 105, 2020, doi: 10.3390/met10010105.

[2] J.-K. Hwang and Y.-C. Chang, "Effects of contact conditions at wire–die interface on temperature distribution during wire drawing," Processes, vol. 11, no. 2, Art. no. 513, 2023, doi: 10.3390/pr11020513.

[3] Y. Shin, B. Hong, S. Chung, W. Chung, and M. Joun, "Accurate finite element simulation of unidirectional and alternate multi-pass drawings, focusing on residual stresses," Appl. Sci., vol. 16, no. 4, Art. no. 2154, 2026, doi: 10.3390/app16042154.

[4] M. Suliga, P. Szota, J. Kulasa, A. Brudny, and M. Burdek, "Friction and wear of tungsten carbide dies in the dry drawing of steel wire," Materials, vol. 18, no. 7, Art. no. 1409, 2025, doi: 10.3390/ma18071409.

[5] M. Suliga, R. Wartacz, and M. Hawryluk, "The multi-stage drawing process of zinc-coated medium-carbon steel wires in conventional and hydrodynamic dies," Materials, vol. 13, no. 21, Art. no. 4871, 2020, doi: 10.3390/ma13214871.

[6] M. Suliga, R. Wartacz, M. Hawryluk, and J. Kostrzewa, "The effect of drawing in conventional and hydrodynamic dies on structure and corrosion resistance of hot-dip galvanized zinc coatings on medium-carbon steel wire," Materials, vol. 15, no. 19, Art. no. 6728, 2022, doi: 10.3390/ma15196728.

[7] J. C. del Rey, G. Guerrero-Vacas, M. Ochoa-Rodríguez, and O. Rodríguez-Alabanda, "Effect of die design and lubricant on ZnAl15% wire drawing: An experimental approach with pressure/hydrodynamic and conventional drawing dies," Lubricants, vol. 13, no. 11, Art. no. 481, 2025, doi: 10.3390/lubricants13110481.

[8] S. Alexandrov, Y.-M. Hwang, and H. S. R. Tsui, "Determining the drawing force in a wire drawing process considering an arbitrary hardening law," Processes, vol. 10, no. 7, Art. no. 1336, 2022, doi: 10.3390/pr10071336.

[9] M. A. Nwir, "Plasto-hydrodynamic pressure in a simple tapered and combined geometry units for drawing and coating wires," Ph.D. dissertation, Dublin City Univ., 1994. [Online]. Available: https://doras.dcu.ie/19520/

[10] S. Akter and M. S. J. Hashmi, "Modelling of the pressure distribution within a hydrodynamic pressure unit: Effect of the change in viscosity during drawing of wire coating," J. Mater. Process. Technol., vol. 77, nos. 1–3, pp. 32–36, 1998, doi: 10.1016/S0924-0136(97)00389-0.

[11] S. Akter and M. S. J. Hashmi, "Wire drawing and coating using a combined geometry hydrodynamic unit: Theory and experiment," J. Mater. Process. Technol., vol. 178, nos. 1–3, pp. 98–110, 2006, doi: 10.1016/j.jmatprotec.2006.02.010.

[12] M. A. Nwir and M. S. J. Hashmi, "Hydro-dynamic pressure distribution in tapered, stepped parallel bore and complex geometry pressure units: Experimental results," J. Mater. Process. Technol., vol. 77, nos. 1–3, pp. 294–299, 1998, doi: 10.1016/S0924-0136(97)00431-7.

[13] S. Gouran, "Numerical investigation on heat transfer characteristics of the viscoelastic fluid flow during wire coating process," Results Eng., vol. 21, Art. no. 101783, 2024, doi: 10.1016/j.rineng.2024.101783.

[14] K. Nabudda, N. Booprempree, W. Ritthong, K. Cheyaksorn, S. Intasonti, and P. Poungthong, "Wire coating in eccentric geometry with fluid and solid interaction using 3D simulation by CFD," Case Stud. Therm. Eng., vol. 74, Art. no. 106748, 2025, doi: 10.1016/j.csite.2025.106748.

[15] M. Suliga, R. Wartacz, J. Kostrzewa, and M. Hawryluk, "Assessment of the possibility of reducing energy consumption and environmental pollution in the steel wire manufacturing process," Materials, vol. 16, no. 5, Art. no. 1940, 2023, doi: 10.3390/ma16051940.

[16] J. Lowrie and G. Ngaile, "Analytical modelling of hydrodynamic lubrication in a multiple-reduction drawing die," Procedia Manuf., vol. 5, pp. 707–723, 2016, doi: 10.1016/j.promfg.2016.08.058.

[17] L. V. Radionova, D. V. Gromov, R. A. Lisovskiy, and I. N. Erdakov, "Experimental determination and calculation of the wire drawing force in monolithic dies on straight-line drawing machines," Machines, vol. 11, no. 2, Art. no. 252, 2023, doi: 10.3390/machines11020252.

[18] M. Pusterhofer, P. Bergmann, F. Summer, F. Grün, and C. Brand, "A novel approach for modelling surface effects in hydrodynamic lubrication," Lubricants, vol. 6, no. 1, Art. no. 27, 2018, doi: 10.3390/lubricants6010027.